JOURNAL OF SYNCHROTRON RADIATION
ISSN 1600-5775

Design, development and first experiments on the X-ray imaging beamline at Indus-2 synchrotron source RRCAT, India

A. K. Agrawal,* B. Singh, Y. S. Kashyap, M. Shukla, P. S. Sarkar and Amar Sinha

Neutron and X-ray Physics Division, Bhabha Atomic Research Centre, Mumbai 85, India.
*Correspondence e-mail: ashishka@rrcat.gov.in

Received 21 November 2014
Accepted 31 August 2015

Edited by I. Schlichting, Max Planck Institute for Medical Research, Germany

Keywords: imaging beamline; X-ray imaging; tomography; phase contrast imaging; micro-tomography.

A full-field hard X-ray imaging beamline (BL-4) was designed, developed, installed and commissioned recently at the Indus-2 synchrotron radiation source at RRCAT, Indore, India. The bending-magnet beamline is operated in monochromatic and white beam mode. A variety of imaging techniques are implemented such as high-resolution radiography, propagation- and analyzer-based phase contrast imaging, real-time imaging, absorption and phase contrast tomography *etc.* First experiments on propagation-based phase contrast imaging and micro-tomography are reported.

1. Introduction

In the last few decades, the availability of third-generation synchrotron sources has initiated revolutionary advances in X-ray imaging. Several new techniques have been discovered such as phase contrast imaging and micro-tomography, coherent diffraction imaging, real-time imaging, fluorescence imaging and *in situ* imaging. Although some of the techniques can be implemented using table-top laboratory-based X-ray sources, synchrotrons are ideally suited for the implementation of the phase-sensitive techniques. With high brilliance, coherence and energy tunability, synchrotron sources allow faster image acquisition, better sensitivity and higher resolution. Moreover, even existing techniques like X-ray absorption contrast imaging can benefit from the improved brilliance of synchrotron sources and allow studies of time-dependent phenomena (Deville *et al.*, 2013; Diemoz *et al.*, 2013; Pereira *et al.*, 2007; Zhong *et al.*, 2000). Synchrotron X-ray imaging techniques are being applied to solve a variety of problems in material science and biology. The internal micro-structure of advanced materials such as composites, foams, bio-materials *etc.* can be visualized non-destructively and quantified to optimize their fabrication. Further, this can be used in the study of mechanical and transport properties of materials through structure property relation. Synchrotron-based X-ray imaging is also useful for the characterization of geological structures and micro-fossils and non-destructive visualization of electronic components. Granular packing of non-equilibrium systems, growth and formation of bone and cartilage, small animal imaging, soft tissue research for cancer diagnostics, and mammography are some other fields of applications (Gastaldi *et al.*, 2012; Chateau *et al.*, 2011; Judex *et al.*, 2010; Westneat *et al.*, 2008; Moffat *et al.*, 2007; Nunan *et al.*, 2006).

In view of the increasing interest, demand and applications of synchrotron X-ray imaging from the scientific community, a

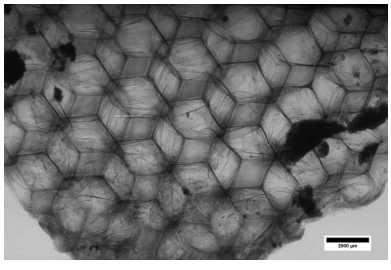

full-field hard X-ray imaging beamline has been designed, developed, installed and commissioned at the Indus-2 synchrotron source. The beamline serves as a national facility and is routinely used for X-ray imaging-based research in material and bio-medical sciences. This article reports the design, specifications and commissioning of the imaging beamline. Important results of beam characterization and feasibility experiments on propagation-based phase contrast imaging and micro-tomography are also described.

2. Beamline overview

2.1. Indus-2 source

Indus-2 is a 2.5 GeV, 300 mA third-generation synchrotron radiation source, with a critical wavelength of 2 Å (Sahni *et al.*, 2009; Tiwari *et al.*, 2013). At present, Indus-2 is being operated at 2.5 GeV energy and 150 mA current. It comprises a double-bend-achromatic lattice with zero dispersion function along the straight sections. This yields a low-emittance and high-brightness photon source for the bending magnets. The estimated photon source size (FWHM) for the Indus-2 bending magnets is 120 µm (V) × 546 µm (H) at 10 keV X-ray energy.

2.2. Beamline description

The imaging beamline (BL-4) is installed at a 10° port of a bending magnet (DP-2) of Indus-2, the synchrotron source at Raja Ramanna Centre of Advanced Technology, Indore, India. The beamline is designed to operate in monochromatic as well as white beam mode. Important beamline parameters are summarized in Table 1. The optical layout of the beamline and the distances of its major components from the tangent point are shown in the Fig. 1. The beamline consists of front-end, optics hutch, experimental station and control room. The front-end design of all the bending-magnet beamlines in the Indus-2 complex is identical and has been reported elsewhere (Raghuvanshi *et al.*, 2007).

2.2.1. Beamline optics. The optics hutch of the beamline consists of all components required for beam shaping, diagnostics and energy tunability. It starts with a beryllium (Be) window of dimensions 105 mm × 15 mm × 0.4 mm at 17.5 m from the tangent point. The beryllium foil (99.8% pure) has a surface roughness of 0.1 µm RMS. It is diffusion bonded to a water-cooled copper body and designed to withstand 180 W heat load. The beryllium window separates the front-end of the beamline from the optical elements. After the beryllium window, a blade beam position monitor is installed to measure the beam position and stability. It consists of two pairs of photosensitive pyro-carbon blades placed across the beam to allow measurement of the generated photoelectron current and trace beam movement as small as 1 µm. Next to this, a pair of entrance slits having tungsten carbide blades is used for shaping the white beam as per the experimental requirements.

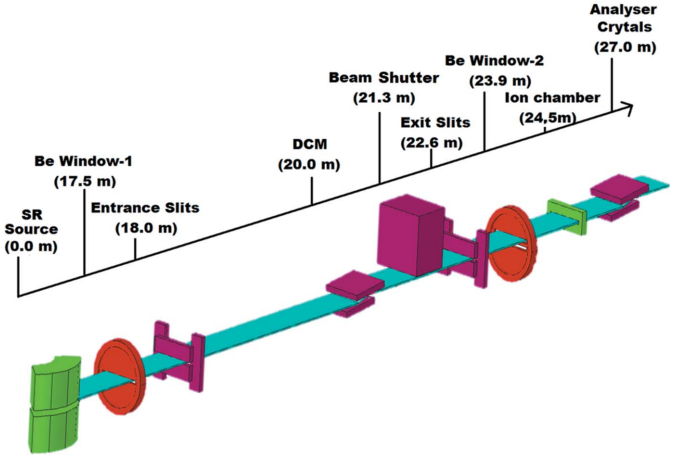

Figure 1
Optics layout of the imaging beamline showing the relative distance of each component from the tangent point.

Table 1
Beamline parameters.

Parameters	Typical values
Source	Bending magnet, 1.5 T dipole
Operational modes	White and monochromatic
Monochromator	Si(111) DCM
Energy range	8–35 keV
Energy resolution	3.86×10^{-3} @ 12 keV in monochromatic mode
Beamline acceptance	5.5 mrad (H) × 0.5 mrad (V)
Photon flux	$\sim 1.74 \times 10^{8}$ photons s^{-1} mm^{-2} $(120\ mA)^{-1}$ at 12 keV monochromatic energy and 25 m from the tangent point 10^{16} photons s^{-1} (white beam)
Sample stage	Five-axis (two-dimensional translation + two-dimensional tilt + one circle rotation)
Detectors	CCD detector, flat panel detector, X-ray microscope, imaging plate, photodiode
Detectors stage	Three-axis manipulator for detectors (*XYZ* translation)

For selecting the desired energy of the monochromatic beam in the energy range (8–35 keV), the beamline uses a double-crystal monochromator (DCM) with a pair of Si (111) crystals. The DCM is required for implementation of the diffraction enhanced imaging technique because identical crystals are used as the analyzer in the experimental station. The first crystal, having an optical area of 140 mm × 100 mm and 10 mm depth, is indirectly rear cooled with water. The second crystal, with an optical area of 160 mm × 140 mm and 20 mm depth, does not have any cooling attachment. The diffracting face of both crystals is polished and strain-free with orientation accuracy of $\sim \pm 0.05°$. The large crystals allow acceptance of the full fan of the incident beam at all Bragg angles over the entire energy range. Optical flatness is within 2 µrad to give a FWHM of the rocking curve within 5% of the theoretical value for the range 8–35 keV. The desired energy is selected by rotating the crystal, thereby varying the Bragg angle. The beam bounces off the diffracting face of the second crystal and leaves the monochromator parallel to the input beam with an upward offset of 25 mm. The use of perpendicular and parallel translation stages allows the fixed-exit capability of the beam to be retained. A provision to lower the first crystal is designed in the monochromator to allow passage of the white beam without changing its spectrum.

All components of the optics hutch downstream of the DCM are designed to allow monochromatic as well as white

Table 2
Different experimental techniques at the imaging beamline.

Hard X-ray imaging techniques	Monochromatic mode	White beam mode
Absorption contrast micro-imaging	Yes	Yes
In-line phase contrast imaging	Yes	Yes
Diffraction enhanced imaging	Yes	No
X-ray micro-tomography (absorption and phase contrast)	Yes	Yes
Laminography	Yes	Yes
Dual energy imaging	Yes	No
Real-time imaging	Yes	Yes

beam mode operation of the beamline. A safety shutter with tungsten block of dimensions 180 mm × 80 mm and 200 mm thickness is used as a beam shutter for both synchrotron and bremsstrahlung radiation. A pair of exit slits having tungsten carbide blades is used for further shaping of the monochromatic and white beam as per the experimental requirements. Both the monochromatic and white beam slits allow systematic opening of the beam aperture up to 140 mm (H) and 60 mm (V). The slit blades have been coated with 100 µm-thick X-ray fluorescent material (Y_2O_3) which is used for online monitoring of the beam shape and size. The beam intensity profile can also be measured with the help of a slit and ion chamber combination. The optics hutch of the beamline is terminated by a pair of beryllium windows of dimensions 140 mm × 15 mm × 0.4 mm separated by 25 mm to allow monochromatic and white beam exit. Both exit Be windows have been coated with aluminium to prevent the oxidation of beryllium during white beam operation. Next to the beryllium windows, an ionization chamber for online monochromatic beam intensity monitoring and a fast shutter for controlled irradiation of live samples have been installed. The ion chamber with a 50 mm-long electrode, 140 mm × 15 mm aperture size and 18 mm electrode separation is operated at a potential up to 1.7 kV and pressure range 0.7–1.3 bar absolute. It is filled with either nitrogen or argon. The fast shutter has a maximum speed of 2500 r.p.m. and opening/closing time of 20 ms, hence a minimum controlled exposure of duration ∼50 ms can be achieved. All components of the beamline up to the exit Be window are operated in ultra-high vacuum (10^{-9} mbar). Major components of the beamline are water-cooled and their temperatures are measured continuously *via* thermocouples installed in the respective devices. The data are used as feedback for the equipment protection system of the beamline.

2.2.2. Experimental station. The imaging beamline is designed to implement a wide range of advanced X-ray micro-imaging techniques such as absorption contrast imaging, propagation-based and diffraction-enhanced phase contrast imaging, micro-tomography, real-time imaging, dual energy imaging *etc*. A list of experimental techniques implemented and available for users is given in Table 2. The experimental station shown in Fig. 2 consists of all the instruments required to perform various imaging experiments such as translation and rotation stages for sample and detector positioning and alignment, imaging detectors, vibration-free optical tables *etc*.

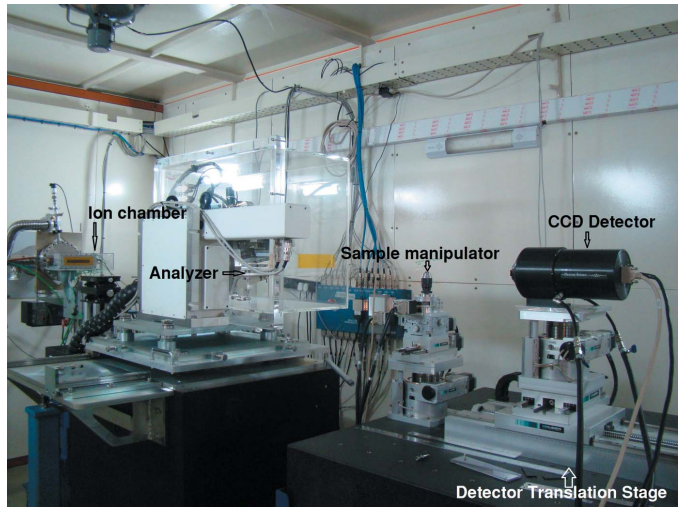

Figure 2
Imaging beamline end-station showing the detector and manipulation stages.

A pair of analyzer Si (111) crystals required for diffraction-enhanced X-ray imaging experiments has also been installed. The analyzer is designed for energies of 8–35 keV with Si (111) crystals with an offset of 25 mm upwards. It acts as a very narrow angular slit, reflecting only the rays that make the correct Bragg angle with the atomic planes of the crystal. It converts the angular distribution in the transmitted beam from the sample into intensity variation in the image and removes all scattered photons from the X-ray beam. Diffraction-enhanced images can be acquired by adjusting the analyzer crystal at various positions on its rocking curve. By using two crystals instead of one, there is no need to have the scanning of the sample or positioning the detector in opposite directions as there is no net beam inversion. For tomography and phase contrast imaging applications the sample is positioned and aligned using a five-axis sample manipulator system. It consists of one full circle rotation stage (360° travel range and 0.001° resolution), two-dimensional tilt stage (±20° travel range and 1″ resolution) and high-precision translation stages to move the sample perpendicular to the beam propagation (travel range 100 mm, accuracy 0.1 µm).

X-ray micro-imaging and tomography in absorption and phase contrast mode is carried out using a Photonic Science VHR-11 camera. The system consists of a 1:2 fibre-optics plate coated with Gadox scintillator and high-resolution CCD (pixels 4007 × 2678, pixel size 4.5 µm and field of view 18 mm × 12 mm). The performance of the camera is linear in the energy range 5–50 keV. In order to image samples of larger dimensions, a flat panel detector (Hamamatsu C7942CA-22) having an imaging area of 120 mm × 120 mm with pixel size ∼50 µm is used. Two separate lens-coupled X-ray imaging microscopes are used for the monochromatic and white beam imaging. The monochromatic camera system uses YAG:Ce scintillators with 5–300 µm thicknesses, objectives lenses of 1.25× to 20× magnifications and a PCO-2000 camera. Various objectives are used for optimizing resolution (800 nm to 12 µm) and field of view (0.7 mm to 12 mm) of the system

Table 3
Resolution and field of view of the X-ray microscope with different objective lenses used with the PCO-2000 camera.

Microscope objective	Optical resolution (μm)	Resolution with scintillators (μm)	Maximum field of view (mm × mm)
1.25×	12	15	12.1 × 12.1
2×	7.8	10	7.6 × 7.6
4×	3.5	3	3.8 × 3.8
10×	1.5	1.8	1.5 × 1.5
20×	0.78	0.8	0.76 × 0.76

as per the experimental requirement. The efficiency of the camera depends on the incident beam energy and the scintillator being used. The achievable resolution and maximum field of view for the monochromatic microscope with different objective lenses and PCO-2000 camera are listed in Table 3. For white beam imaging the microscope uses a tungsten shield for objective lens protection and a thicker scintillator for heat load compatibility. The absorption efficiency of the YAG:Ce scintillator being used in the white beam detector decreases with energy and increases with thickness. The spectrum of the incident white beam at the sample position is shown in Fig. 3. The energy ranges from 5 to 40 keV and peaks at nearly 10 keV. The sensitivity of the white beam detector is optimized using a 300 μm-thick scintillator which has approximately 99.5% absorption efficiency at 10 keV. Objectives of 2×, 5× and 10× are used with this scintillator in the white beam microscope. A micro-CT compression and tensile stage with load cells of 500 N and 3 kN has also been installed for *in situ* micro-imaging and tomography experiments which is currently available only for white beam mode. All the components in the experimental hutch are installed over a vibration-isolated optical table to avoid image smearing due to system instabilities.

2.2.3. Data acquisition and analysis. The beamline control system allows operational control and parameter setting of the optics, motion stages, detectors and beam diagnostics components. It also consists of a data acquisition system, equipment protection system (EPS) and personal safety system (PSS). The EPS is designed to operate beamline components in safe conditions and circumvents accidental heating, vacuum failure or contamination, whereas PSS is designed for personal protection against exposure to radiation, hazardous gases and high voltage. The beamline uses a GPU-based multicore computing facility for tomography data reconstruction and visualization. An image processing and image analysis facility to extract quantitative structure and density information from tomographic images is also available as per the requirements. A phase-retrieval facility is available to obtain quantitative phase information from phase contrast X-ray images (Kashyap *et al.*, 2009, 2010*a*,*b*, 2011; Yadav *et al.*, 2008).

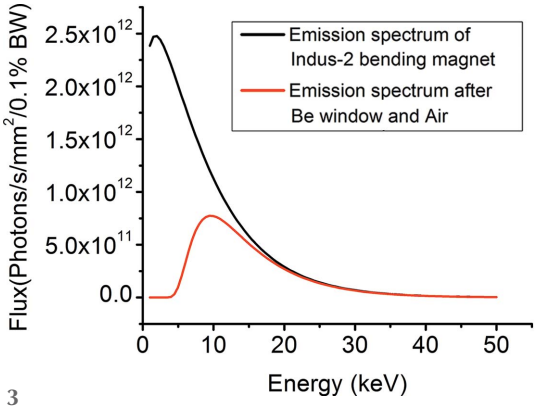

Figure 3
Calculated spectra of synchrotron white beam from a bending magnet before and after attenuation caused by beamline components and air.

3. Results and discussion

3.1. Measurement of beam characteristics

The intrinsic characteristics of a synchrotron beam such as high brilliance and energy tunability provide significant improvements in image quality (Koch *et al.*, 1983). Prior knowledge of system parameters such as energy-dependent variation of beam size, divergence, flux density, beam uniformity, energy resolution ($\Delta E/E$) of the DCM, spatial resolution of various imaging detectors is necessary before planning of the imaging experiments. Theoretical calculations using *XOP* (Del Rio & Dejus, 2011) and experimental measurements of these properties were carried out for the imaging beamline.

3.1.1. Beam divergence and flux. *White beam mode.* In the case of white beam mode the integrated beam flux was calculated to be 1.7×10^{16} photons s^{-1} using *XOP*. Fig. 3 compares the emission spectrum (energy range 1–50 keV) of synchrotron radiation from a bending-magnet source and its modification due to absorption losses in the beryllium windows and air path in the experimental station. The beam opening angle variation is shown in Fig. 4(*a*). The beam profile is measured by scanning the small vertical aperture (300 μm) in the entrance slit against the ion chamber current as shown in Fig. 4(*b*). The beam size was measured to be 4.5 mm FWHM at 18 m from the source point which is in accordance with the theoretical value.

Monochromatic beam mode. The peak flux and divergence of the monochromatic beam decreases with increasing photon energy. Experimental measurement of the vertical beam size was carried out at 18 m from the source using slit aperture scanning against ion chamber current and calculating the FWHM of Gaussian profile. The beam sizes are in good agreement with theoretical data as shown in Fig. 5. The peak flux density at all energies was measured at 25 m from the source using a calibrated silicon photodiode AXUV100 (IRD, USA). Fig. 6 shows a comparison of calculated and experimental flux density at various energies. The calculated flux at 12 keV is 4.98×10^8 photons s^{-1} mm^{-2} $(120\ mA)^{-1}$ whereas the measured flux is 1.74×10^8 photons s^{-1} mm^{-2} $(120\ mA)^{-1}$. The difference in measured and calculated flux is attributed to the attenuation and scattering losses in the beamline optical components such as beryllium windows, DCM crystals, ion chamber and air in the propagation path of the beam from its source to the experimental station. Transmission of a 12 keV

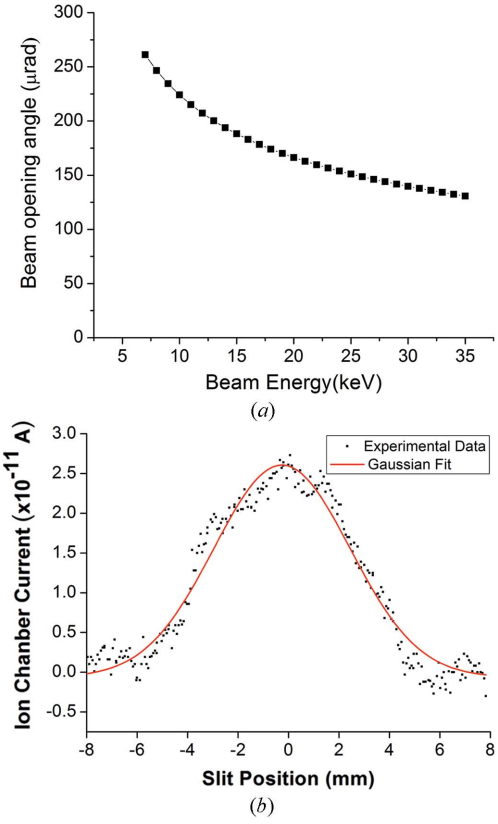

Figure 4
(*a*) Variation of beam divergence with energy. (*b*) White beam vertical profile. FWHM of the profile was measured as 4.5 mm.

beam through 2 × 0.4 mm of beryllium is 93%; through 10 cm argon (ion chamber) it is 37%. Therefore the calculated flux × 0.93 × 0.37 = 1.71 × 10^8 photons s^{-1} mm^{-2} $(120\ mA)^{-1}$ is quite comparable with the measured flux.

3.1.2. Beam uniformity. A direct beam image acquired at 12 keV using a high-resolution CCD detector is shown in Fig. 7(*a*). The variation of intensity along the horizontal and vertical directions is shown in the figure along with its histogram to show beam uniformity. There seems to be some variations in the image grey values (FWHM ≃ 14.7%) which are attributed to the fibre-optic structure in the CCD image and non-linear response of various pixels. For imaging application a flat-field correction is applied to correct these effects. Fig. 7(*b*) shows the flat-field-corrected image along with its horizontal and vertical profiles and histogram. The beam uniformity is significantly improved after flat-field correction (FWHM ≃ 4%).

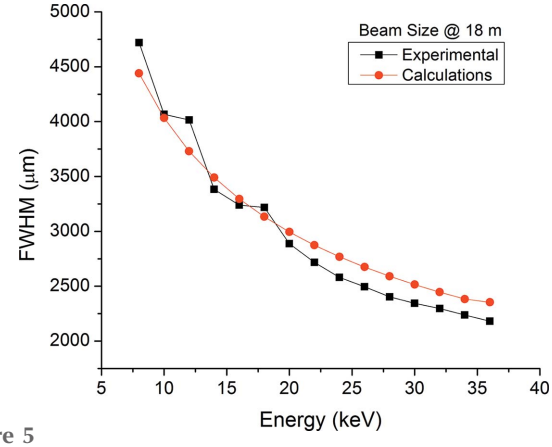

Figure 5
Monochromatic beam vertical size variation with photon energy.

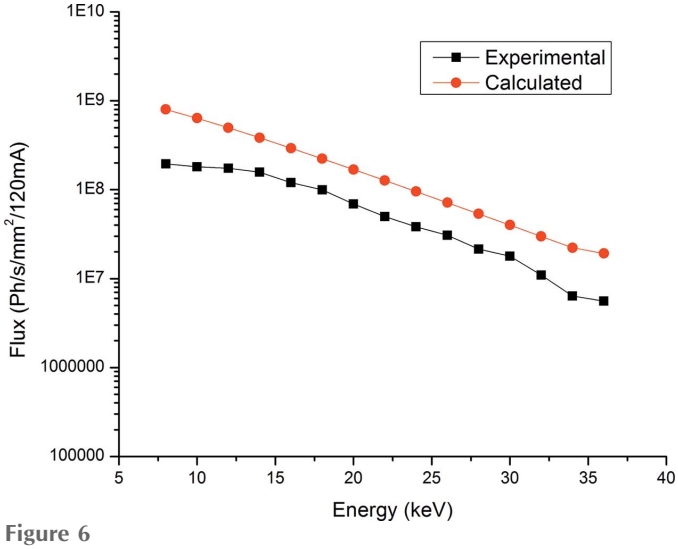

Figure 6
Monochromatic beam flux variation with photon energy.

3.1.3. Beam monochromaticity. The intrinsic energy resolution ($\Delta E/E$) of silicon ⟨111⟩ is 1.2 × 10^{-4} for a perfectly collimated beam. The energy resolution of the DCM was measured using its rocking curve as shown in Fig. 8. The FWHM of the rocking curve is 53.5 μrad at 12 keV; hence, the energy resolution at this energy is measured to be 3.2 × 10^{-4}. The difference in intrinsic and measured energy resolution is attributed to the beam divergence (Schilling *et al.*, 1995). As shown in Fig. 4(*a*), the beam divergence is decreasing with increasing photon energy. This improves the energy resolution at higher energies.

3.2. Measurement of detector resolution

The spatial resolution of the two most popularly used detectors at the imaging beamline was measured using JIMA resolution pattern RC RT02B (http://www.jima.jp). For the fibre-optic coupled CCD camera the resolution was measured to be 5 μm with 8% contrast. Line segments up to 5 μm intervals can be visualized clearly in the image acquired using a 15 keV monochromatic beam and 800 ms exposure time as shown in Fig. 9(*a*) which is in line with the intrinsic resolution of the camera with pixel size 4.5 μm and 2× magnification. Similarly the resolution of the lens-coupled high-resolution X-ray microscope was also measured with a 50 μm-thick YAG scintillator and 4× objective. The image was acquired at 15 keV with an exposure time of 120 s. Line segments of 3 μm are visible with 20% contrast, hence the resolution of the system with this combination is ∼3 μm as shown in Fig. 9(*b*).

3.3. Imaging experiments

In the initial phase, absorption contrast micro-imaging, propagation-based phase contrast imaging and tomography

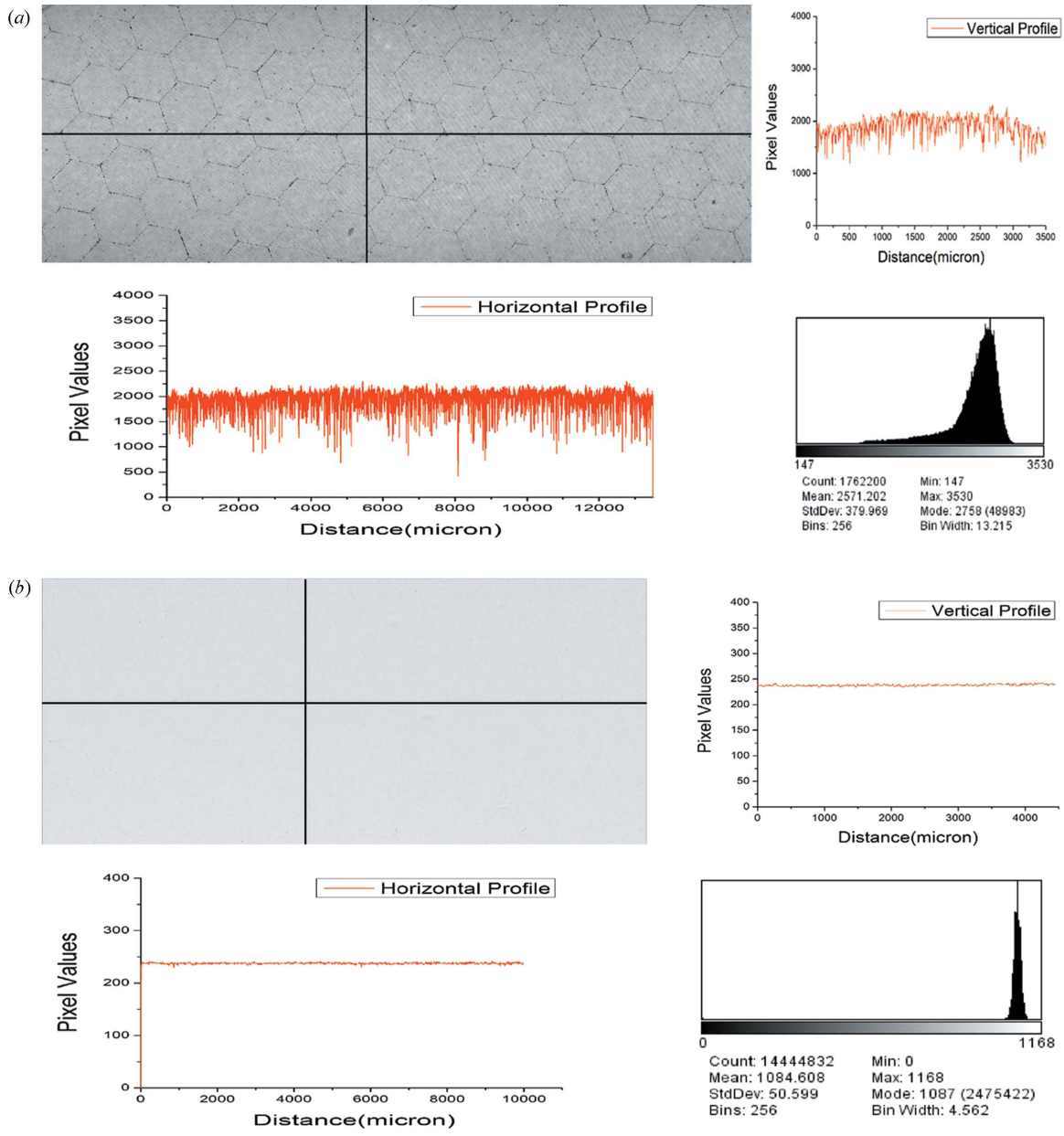

Figure 7
(*a*) Flat-field image of the synchrotron beam at 12 keV acquired using a fibre-optic-coupled CCD detector showing beam uniformity. The figure also shows the horizontal and vertical profile plots of the image grey values and its histogram. (*b*) Flat-field-corrected image of the beam in high-resolution CCD and its grey value histogram. The figure also shows horizontal and vertical profile plots of image grey values and its histogram.

experiments were carried out. Absorption contrast imaging is used to obtain the distribution of the attenuation coefficients for strongly absorbing materials (Stewart *et al.*, 1994). A high-resolution full-field absorption contrast projection image of the Indian bee's beehive is shown in Fig. 10. The image was acquired with a fibre-optic-coupled CCD camera using monochromatic beam at 12 keV for 600 ms exposure time. The resolution of the image is 5 µm. The image shows hexagonal micro-structure of natural fibres in the beehive and entrapped honey within it.

Propagation-based phase contrast imaging provides improved visibility of the interfaces with the possibility of retrieving a quantitative refractive index distribution. After interacting with a weakly absorbing sample, Fresnel diffraction in the parallel monochromatic beam at increasing propagation distances improves edge contrast for visualizing its structural and density variations (Pogany *et al.*, 1997). We have applied this technique to study the multi-layered micro-structure of simulated TRISO (tri-structural isotropic) particles which are potential fuel candidates for high-temperature reactors (Dulera & Sinha, 2008). Figs. 11(*a*) and 11(*b*) show absorption and propagation-based phase contrast images, respectively, acquired at respective propagation distances of 5 mm and 500 mm. The sample contains multiple layers of pyro-carbon (PyC) and silicon carbide (SiC) coatings over a zirconium oxide spherical core of diameter 500 µm in the

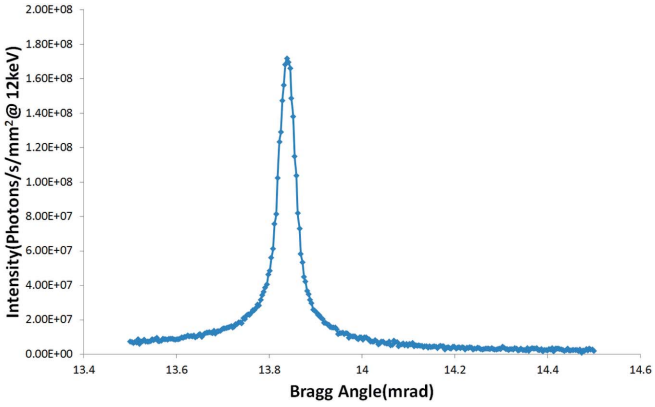

Figure 8
Rocking curve of the DCM at 12 keV. The FWHM of the rocking curve was measured as 53.53 µrad.

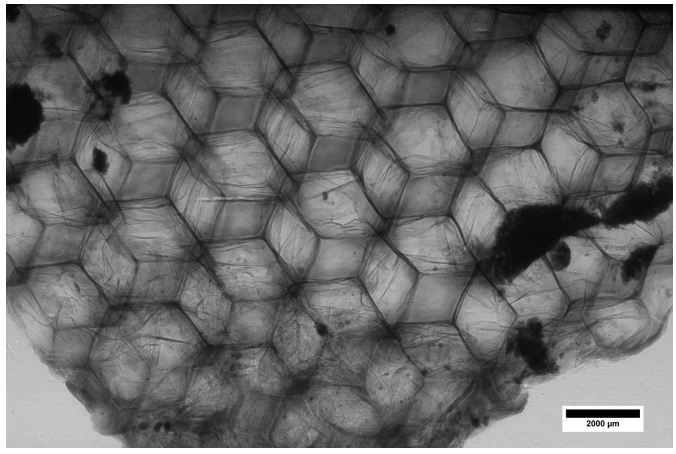

Figure 10
Full-field high-resolution image of a beehive. The field of view is 18 mm × 10 mm; resolution is 4.5 µm.

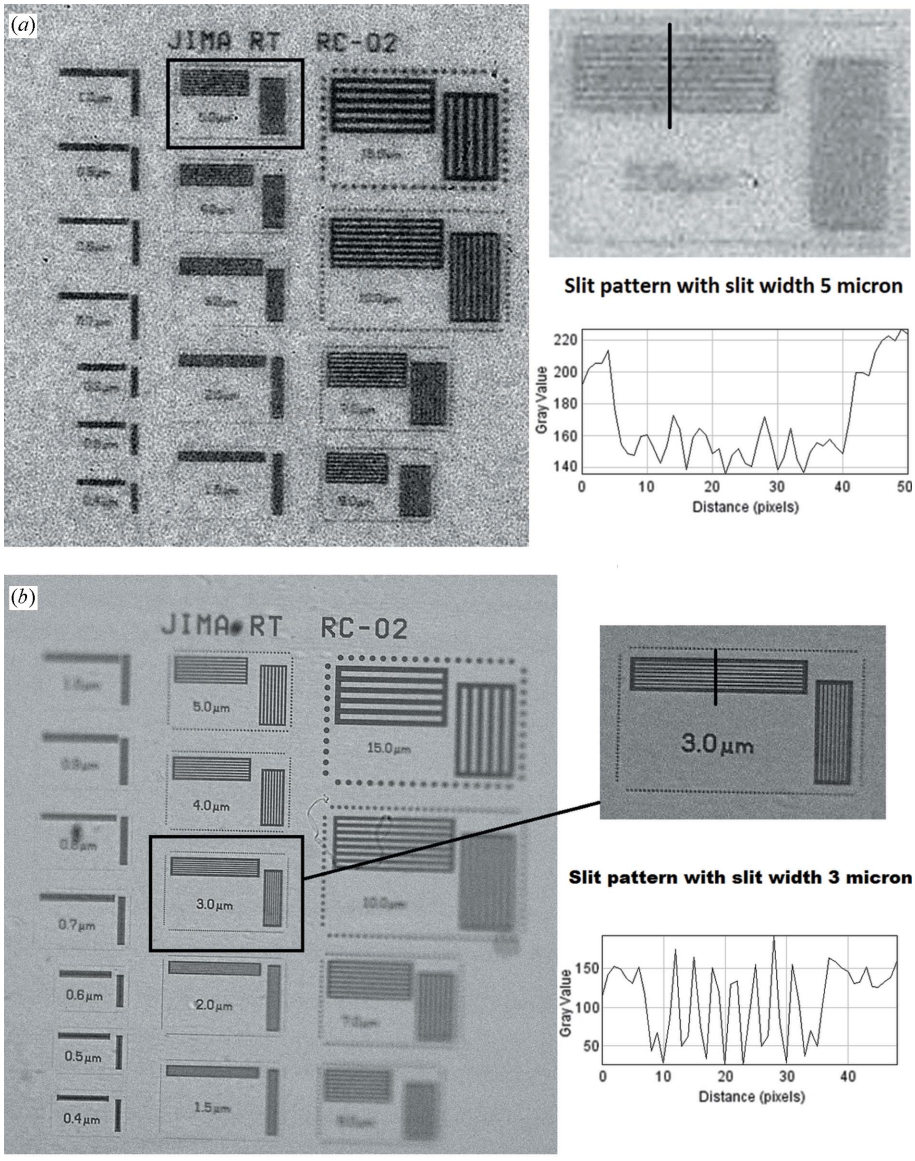

Figure 9
Spatial resolution measurement using the JIMA pattern. (*a*) Fibre-optic-coupled CCD detector. (*b*) Lens-coupled CCD detector.

order shown in Table 4 and Fig. 11(*c*). Table 4 also shows the density and thickness of the coating layers. The phase contrast image offers improved visibility at the layered interfaces. The small density difference between the inner PyC and buffer layer cannot be resolved in the absorption contrast image whereas it is clearly visible in the propagation-based phase contrast image.

Tomography is used for three-dimensional imaging of objects in absorption and phase contrast modes to determine the three-dimensional distribution of the linear attenuation coefficient and refractive index, respectively. X-ray micro-tomography experiments were carried out on a cartilage bone sample to study its micro-structure and explore the feasibility of osteoporosis studies (Stenström *et al.*, 2000). The experiments were performed in phase contrast enhanced projection imaging mode. The data were acquired for 180° rotation of the sample with 0.2° rotation step in parallel beam geometry. 901 projections were collected in addition to reference and background images. The data were preprocessed for image noise and flat-field correction, and then back-projected using a filtered back-projection algorithm of the three-dimensional reconstruction. The projection image and reconstructed slice image of the sample are shown in Figs. 12(*a*) and 12(*b*). While the projection images hardly identify porous micro-structure of the bone, the tomography recon-

Table 4
Density and thickness of coating layers in the TRISO coated fuel particle.

Coating layer	Density (g cm^{-3})	Coating thickness (µm)
Buffer	1.1	95
Inner PyC	1.9	40
SiC	3.18	35
Outer PyC	1.9	40

structed slice image clearly shows the hard bone porous microstructure as well as softer interwoven material. The reconstructed slice image also shows small micro-pores in the walls of the cartilage bone that is not visible at all in the projection image. The three-dimensional volume of the sample was also reconstructed using the *DRISTI* three-dimensional visualization tool (Limaye, 2012). The resulting image, Fig. 12(*c*), shows pores and imperfections in the volume of the sample. The volume was cropped for improved three-dimensional visibility. Quantitative measurement of the porosity and other geometrical parameters of cellular structure are useful in osteoporosis studies which are being planned in the near future (Feng *et al.*, 2011).

4. Access and future developments

The imaging beamline (BL-4) was successfully installed and commissioned at the Indian synchrotron source Indus-2. The facility is open for users from across the world and can be accessed through the Indus beamline user portal. Future plans of the beamline include development and implementation of new imaging techniques such as fluorescence contrast imaging, diffraction contrast microscopy and *in situ* micro-tomography for widening imaging beamline applications. We are also planning to install a double-crystal multilayer monochromator before the DCM. Simulations and instrumentations are under process for development of new phase contrast imaging modes such as grating-based phase contrast and speckle-based phase retrieval.

Acknowledgements

We acknowledge all group members in the Neutron and X-ray Physics Division BARC, Indus Synchrotron Utilization Division and Indus Operation and Accelerator Physics Division RRCAT for their contribution during installation and commissioning of the beamline. We are also grateful to Dr S. Kailas, former Director of Physics group, Dr P. D. Gupta, Director of RRCAT, Dr S. L. Chaplot, Director of Physics group, BARC, and Dr G. S. Lodha, Head, ISUD, RRCAT, for their constant support and valuable input during the project.

References

Chateau, C., Gélébart, L., Bornert, M., Crépin, J., Boller, E., Sauder, C. & Ludwig, W. (2011). *Compos. Sci. Technol.* **71**, 916–924.

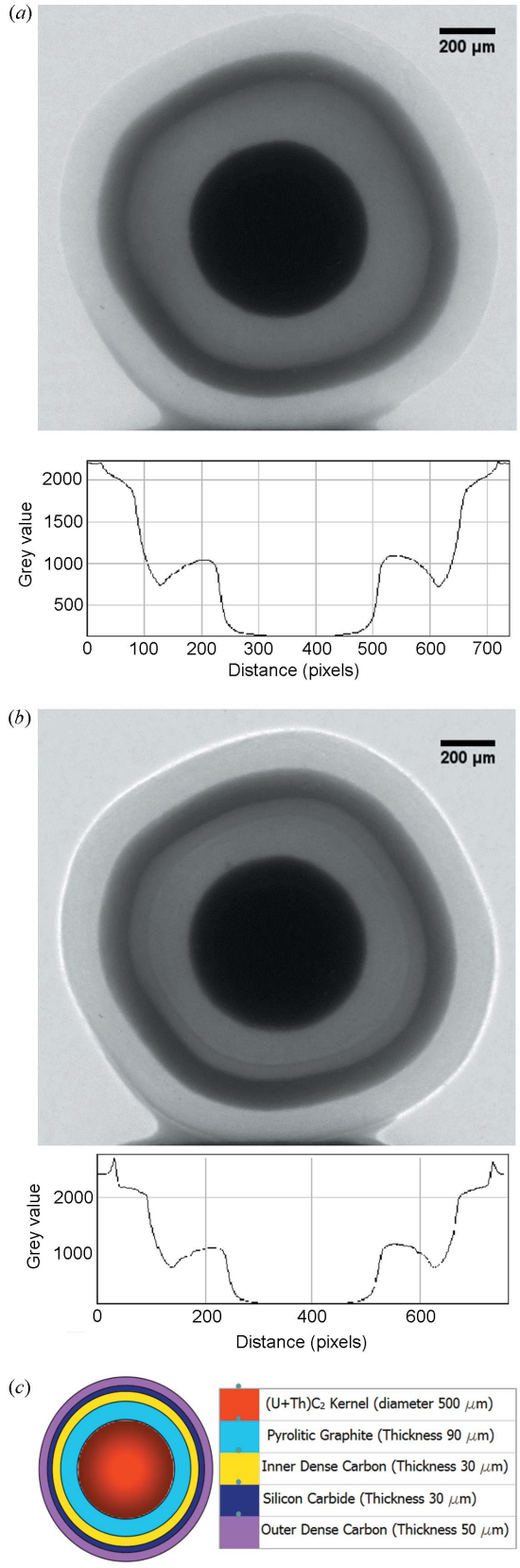

Figure 11
Comparison of the (*a*) absorption contrast and (*b*) propagation-based phase contrast images of a TRISO coated fuel particle. The bottom of the respective images shows a profile plot of the images' central row. (*c*) Schematic design of a TRISO coated fuel particle showing diameters of various coating layers.

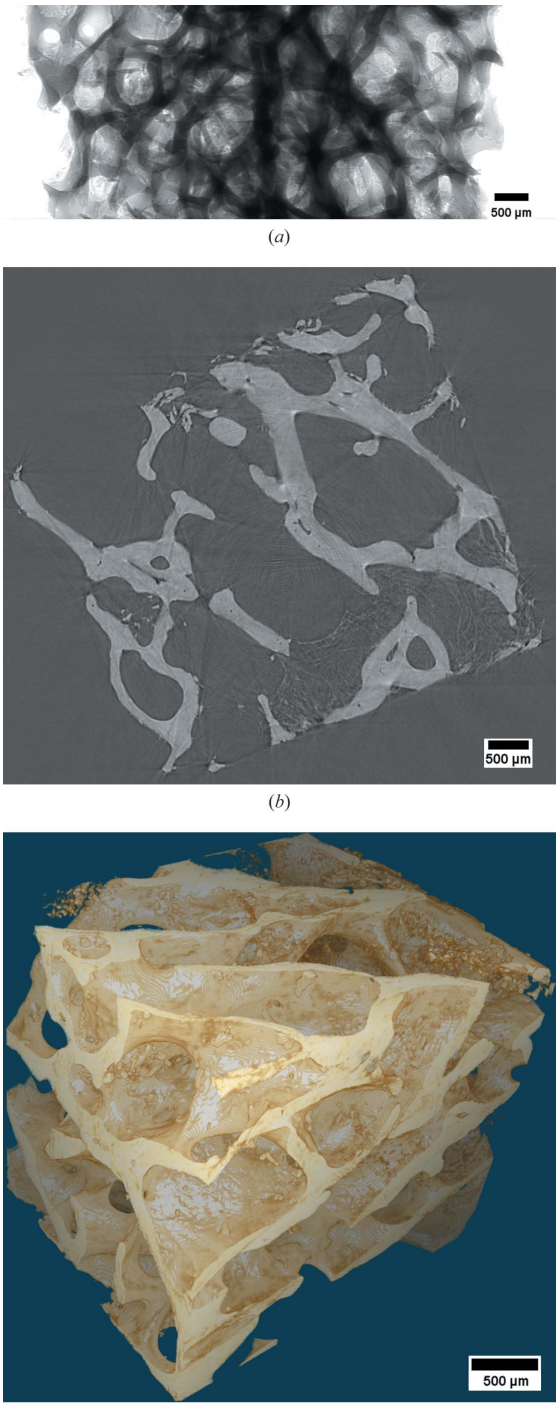

Figure 12
Comparison of the (*a*) absorption contrast projection image and (*b*) micro-tomography reconstructed slice image of bone. (*c*) Three-dimensional volumetric image of bone micro-structure showing the cellular geometry and pores.

Del Rio, M. S. & Dejus, R. J. (2011). *Proc. SPIE*, **8141**, 814115.
Deville, S., Adrien, J., Maire, E., Scheel, M. & Di Michiel, M. (2013). *Acta Mater.* **61**, 2077–2086.
Diemoz, P. C., Endrizzi, M., Zapata, C. E., Pesic, Z. D., Rau, C., Bravin, A., Robinson, I. K. & Olivo, A. (2013). *Phys. Rev. Lett.* **110**, 138105.
Dulera, I. V. & Sinha, R. K. (2008). *J. Nucl. Mater.* **383**, 183–188.
Feng, Y., Feng, Z., Li, S., Zhang, W., Luan, X., Liu, Y., Cheng, L. & Zhang, L. (2011). *Composites A*, **42**, 1645–1650.
Gastaldi, D., Canonico, F., Capelli, L., Boccaleri, E., Milanesio, M., Palin, L., Croce, G., Marone, F., Mader, K. & Stampanoni, M. (2012). *Constr. Build. Mater.* **29**, 284–290.
Judex, S., Luu, Y. K., Ozcivici, E., Adler, B., Lublinsky, S. & Rubin, C. T. (2010). *Methods*, **50**, 14–19.
Kashyap, Y. S., Agrawal, A., Sarkar, P. S., Shukla, M., Roy, T. & Sinha, A. (2010*a*). *J. Synchrotron Rad.* **17**, 799–803.
Kashyap, Y. S., Agrawal, A., Sarkar, P. S., Shukla, M., Roy, T. & Sinha, A. (2011). *NDT Intl*, **44**, 41–46.
Kashyap, Y. S., Agrawal, A., Sarkar, P. S., Shukla, M., Roy, T., Sinha, A., Aswal, D. K. & Debnath, A. K. (2010*b*). *AIP Conf. Proc.* **1313**, 149–151.
Kashyap, Y. S., Yadav, P. S., Sarkar, P. S., Agrawal, A., Roy, T., Sinha, A., Dasgupta, K. & Sathiyamoorthy, D. (2009). *NDT Intl*, **42**, 384–388.
Koch, E. E., Eastman, D. E. & Farges, Y. (1983). *Handbook of Synchrotron Radiation*, Vol. 1a, edited by E. E. Koch, ch 1. Amsterdam: North-Holland.
Limaye, A. (2012). *Proc. SPIE*, **8506**, 85060X.
Moffat, A. J., Mellor, B. G., Sinclair, I. & Reed, P. A. S. (2007). *Mater. Sci. Technol.* **23**, 1396–1401.
Nunan, N., Ritz, K., Rivers, M., Feeney, D. S. & Young, I. M. (2006). *Geoderma*, **133**, 398–407.
Pereira, G. R., Rocha, H. S., Anjos, M., Faria, P., Pérez, C. A. & Lopes, R. T. (2007). *Nucl. Instrum. Methods Phys. Res. A*, **581**, 128–132.
Pogany, A., Gao, D. & Wilkins, S. W. (1997). *Rev. Sci. Instrum.* **68**, 2774–2782.
Raghuvanshi, V. K., Dhamgaye, V. P., Singh, A. K. & Nandedkar, R. V. (2007). *AIP Conf. Proc.* **879**, 631–634.
Sahni, V. C., Chia, S., Ratnavelu, K. & Muhamad, M. R. (2009). *AIP Conf. Proc.* **1150**, 180–187.
Schilling, P. J., Morikawa, E., Tolentino, H., Tamura, E., Kurtz, R. L. & Cusatis, C. (1995). *Rev. Sci. Instrum.* **66**, 2214–2216.
Stenström, M., Olander, B., Lehto-Axtelius, D., Erik Madsen, J., Nordsletten, L. & Alm Carlsson, G. (2000). *J. Biomech.* **33**, 289–297.
Stewart, J. B., Moran, C. J. & McBratney, A. B. (1994). *Develop. Soil Sci.* **22**, 507–514.
Tiwari, M. K., Gupta, P., Sinha, A. K., Kane, S. R., Singh, A. K., Garg, S. R., Garg, C. K., Lodha, G. S. & Deb, S. K. (2013). *J. Synchrotron Rad.* **20**, 386–389.
Westneat, M. W., Socha, J. J. & Lee, W. K. (2008). *Annu. Rev. Physiol.* **70**, 119–142.
Yadav, P. S., Kashyap, Y. S., Roy, T., Sarkar, P. S. & Sinha, A. (2008). *J. Synchrotron Rad.* **15**, 100–105.
Zhong, Z., Thomlinson, W., Chapman, D. & Sayers, D. (2000). *Nucl. Instrum. Methods Phys. Res. A*, **450**, 556–567.